

Measurements of the Net Charge Density of Space Plasmas

Chao Shen^{1,1}, Yufei Zhou^{1,1}, Lai Gao^{1,1}, Zuyin Pu², Xiaogang Wang³, C. Philippe Escoubet⁴, and J. L. Burch⁵

¹School of Science, Harbin Institute of Technology

²School of Earth and Space Sciences, Peking University

³School of Physics, Harbin Institute of Technology

⁴ESA/ESTEC

⁵Southwest Research Institute

November 30, 2022

Abstract

Space plasmas are composed of charged particles that play a key role in electromagnetic dynamics. However, to date, there has been no direct measurement of the distribution of such charges in space. In this study, three schemes for measuring charge densities in space are proposed. The first scheme is based on electric field measurements by multiple spacecraft. This method is applied to deduce the charge density distribution within Earth's magnetopause boundary layer using Magnetospheric MultiScale constellation (MMS) 4-point measurements, and indicates the existence of a charge separation there. The second and third schemes proposed are both based on electric potential measurements from multiple electric probes. The second scheme, which requires 10 or more electric potential probes, can yield the net charge density to first-order accuracy, while the third scheme, which makes use of seven to eight specifically distributed probes, can give the net charge density with second-order accuracy. The feasibility, reliability, and accuracy of these three schemes are successfully verified for a charged-ball model. These charge density measurement schemes could potentially be applied in both space exploration and ground-based laboratory experiments.

Measurements of the Net Charge Density of Space Plasmas

Chao Shen^{1*}, Yufei Zhou¹, and Lai Gao¹, Xiaogang Wang², Zuyin Pu³, C. Philippe
Escoubet⁴, J. L. Burch⁵

¹School of Science, Harbin Institute of Technology, Shenzhen, 518055, China

²School of Physics, Harbin Institute of Technology, Harbin, 150001, China

³School of Earth and Space Sciences, Peking University, Beijing, China⁴ESA/ESTEC
(SCI-SC), Postbus 299, Keplerlaan, 1, 2200 AG Noordwijk, The Netherlands

⁵Southwest Research Institute, San Antonio, TX, USA

Corresponding author: Chao Shen (shenchao@hit.edu.cn)

21

22 **Key Points:**

23 Charge densities in geomagnetopause have been calculated using MMS electric field
24 measurements.

25

26 A method for extracting the charge density from 10-point electric potential
27 measurements is presented.

28

29 An additional scheme to measure the charge density using seven or eight electric
30 potential probes is explored.

31

32

33 **Key Words:**

34 Charge Density, Electric Field, Electric Potential Measurements, Multi-Point
35 Measurements, Magnetopause

36

37

38

39

40

41

42

Abstract

Space plasmas are composed of charged particles that play a key role in electromagnetic dynamics. However, to date, there has been no direct measurement of the distribution of such charges in space. In this study, three schemes for measuring charge densities in space are presented. The first scheme is based on electric field measurements by multiple spacecraft. This method is applied to deduce the charge density distribution within Earth's magnetopause boundary layer using Magnetospheric MultiScale constellation (MMS) 4-point measurements, and indicates the existence of a charge separation there. The second and third schemes proposed are both based on electric potential measurements from multiple electric probes. The second scheme, which requires 10 or more electric potential probes, can yield the net charge density to first-order accuracy, while the third scheme, which makes use of seven to eight specifically distributed probes, can give the net charge density with second-order accuracy. The feasibility, reliability, and accuracy of these three schemes are successfully verified for a charged-ball model. These charge density measurement schemes could potentially be applied in both space exploration and ground-based laboratory experiments.

65

66 **1. Introduction**

67

68 Electromagnetic fields are omnipresent in space. They control the motion of
69 plasmas, and the transportation, release, and transformation of energy in space, and
70 thereby are the key driver of space weather hazards. Charges and electric currents
71 (flows of charged particles) source the electromagnetic field, and therefore the
72 distribution and motions of charges determine its form. Charge separations occur in
73 electric double layers, which exist commonly in space plasmas (Block, 1975; Akasofu,
74 1981; Raadu, 1989). Net charges can appear in plasma boundary layers (Parks, 1991),
75 e.g., the magnetopause boundary layers and Alfvén layers (Hasegawa and Sato, 1989).
76 Charge separations can also occur during ambipolar diffusion processes (Alfvén, 1963;
77 Bittencourt, 2004), e.g., the Earth’s polar wind (Axford, 1968; Lemaire and Pierrard,
78 2001; Yau et al., 2007). In macro-scale plasmas, flow shears or vorticities can
79 accumulate these net charges, driving the field-aligned currents (Michael, 2014).
80 Charge separations also play a key role in plasma instabilities, e.g., the Rayleigh-Taylor
81 instability (Treumann and Baumjohann, 1997; Michael, 2014) and the tearing
82 instability (Treumann and Baumjohann, 1997).
83 The charge separations in space plasmas can appear at various spatial scales. The
84 plasmas with no magnetic field are commonly electrically neutral when the spatial scale
85 is much larger than the Debye length and the temporal scale is rather longer than the
86 plasma oscillation time (Bittencourt, 2004). At the Debye length space scale or plasma

oscillation time scale, the electrical neutrality would be violated and charge separations appear. On the other hand, the ambipolar diffusion takes place in inhomogeneous plasmas due to the different thermal velocities of the electrons and ions, and polarization electric fields will be created, which can span several Earth radii in the Earth's polar wind regions (Axford, 1968; Lemaire and Pierrard, 2001). However, as results of the difference between the parameters of electrons and ions, the charge separations in magnetized plasmas at spatial scales much larger than the Debye length can take place. As for the magnetopause boundary layers, the protons of solar wind can penetrate more deeply into the magnetosphere than electrons because of their greater gyroradius. Therefore, the magnetosphere and magnetosheath sides of the magnetopause boundary layer are positively and negatively charged, respectively, and the width of the magnetopause boundary layer is at the order of proton gyroradius (several hundred Kilometers) (Parks, 1991; Kivelson and Russell, 1995). During the magnetospheric substorms, the plasmas are injected from the magnetotail into the inner magnetosphere, and the ions and electrons are energized and drift duskward and dawnward, respectively. As a result, the duskside and dawnside of the inner magnetosphere accumulate positive and negative charges, respectively, and a dawnward shielding electric field with a spatial scale of several Earth radius is established (Hasegawa and Sato, 1989).

The acquisition of a spatial distribution of electric charge density is of critical importance for recognizing and understanding the dynamics of electromagnetic fields and plasmas in space. However, there is still no equipment available for directly measuring the net charge density in space, although measurements of the charge density in the atmosphere near the ground have been achieved. The difficulty of such measurements in space arises because the plasmas there are extremely thin, with only

a few charged particles per cm^3 , and the net charge density is even lower by several orders. According to Harris (1962), the maximum charge density within the magnetopause boundary layer is $|\rho|_{\max} \approx 2ne(1 - V^2/c^2)^{-2}V^2/c^2$, where n is the number density of the plasmas, V is the drifting velocity of electrons and ions, c is the free speed of light in vacuum. According to Lee and Kan (1979), the main carriers of the current in the magnetopause are ions, whose temperature is about 300 eV and thermal velocity is estimated to be $V \approx 200\text{km/s}$. Assume $n \approx 10\text{cm}^{-3}$ in the magnetopause, then $|\rho|_{\max} \approx 10\text{e/m}^3$.

Cluster mission has first achieved the four-point measurements on the electric field in space (Escoubet et al., 2001), with which the electric field structure of the magnetopause boundary layer has been revealed (Paschmann et al., 2005; Haaland et al., 2021 and references therein). The Magnetospheric MultiScale (MMS) constellation (Burch et al., 2016) can measure the 3-dimensional electric field vector at four locations in space so as to obtain the linear gradient of the electric field. By using this advantage, Tong, et al. (2018) have deduced the spatial distribution of net charge within a magnetic hole and found there are net positive charges in the center of the magnetic hole and an electron sheath around the hole. With a similar approach Argall et al. (2019) have investigated the distribution of charge density in the diffusion region of magnetic reconnection. However, we still have no independent charge density measurement equipment in space. In this article, we will explore how the charge density can be deduced based on multiple-probe electric potential measurements on board a single spacecraft.

In Section 2, we first discuss the method for deducing the charge density from 4-point electric field measurements, which has been applied to analyze the charge density distribution in the dayside magnetopause boundary layer during an MMS

magnetopause crossing event. In Section 3, a method for deducing the charge density from ≥ 10 -point electric potential measurements is studied. Section 4 explores measurements of the charge density based on seven or eight electric potential probes. Section 5 gives a summary and some discussion.

2. Deducing the charge density from multi-spacecraft electric field measurements

The direct approach to obtain the net charge density is to sum up the charge densities of positively and negatively charged particles with the formula

$$\rho = -en_e + \sum_i q_i n_i, \quad (1)$$

where n_e and n_i are the densities of the electrons and the i -th ion, respectively, and q_i is the charge of the i -th ion. However, the electric force is so strong that the plasmas are always quasi-neutral, and the separation between the two types of charges is very slight. Therefore, the charge densities in space plasmas are extremely small. It is almost impossible to determine the net charge density by measuring the densities of charged particles at the present stage of space exploration.

The most feasible and practicable method at present is to deduce the net charge density by measuring the electric potentials or electric fields created by the net charges at high accuracies with well-developed technology (Mozer et al., 1967; Mozer, 1973; Paschmann et al., 1997; Pedersen et al., 1998; Michael, 2014). The Spin-plane Double Probes (SDPs) and Axial Double Probes (ADPs) (Torbert et al., 2016; Lindqvist et al., 2016; Ergun et al., 2016) onboard the four spacecraft of the MMS constellation (Burch et al., 2016) yield four electric field vectors at four different locations separated by tens

of kilometers. With the Gaussian theorem, $\rho = \epsilon_0 \nabla \cdot \mathbf{E}$, we can get the charge density at the center of the constellation, as illustrated in Fig. 1. Suppose that the four spacecraft of the MMS constellation are located at four different positions \mathbf{r}_α ($\alpha = 1, 2, \dots, 4$). The barycenter of the MMS constellation is $\mathbf{r}_c \equiv \frac{1}{4} \sum_{\alpha=1}^4 \mathbf{r}_\alpha$. It is convenient to assume that $\mathbf{r}_c = 0$, so that the barycenter of the constellation is the origin of the frame of reference. The four spacecraft yield four electric fields, $\mathbf{E}_\alpha = \mathbf{E}(\mathbf{r}_\alpha)$, $\alpha = 1, 2, \dots, 4$. Under the linear assumption, the i -th component of the gradient of the electric field at the barycenter can be calculated as (Harvey, 1998; Chanteur, 1998)

$$(\nabla_i \mathbf{E})_c = \frac{1}{4} \sum_{\alpha=1}^4 \mathbf{E}_\alpha \mathbf{r}_{\alpha j} \mathbf{R}_{ji}^{-1}, \quad (2)$$

where $\mathbf{R}_{ij} = \frac{1}{4} \sum_{\alpha=1}^4 r_{\alpha i} r_{\alpha j}$ is the volumetric tensor of the constellation (Harvey, 1998), and \mathbf{R}_{ji}^{-1} its inverse. By using the Gaussian theorem, we can get the charge density with the divergence of the electric field vector, i.e.,

$$\rho = \epsilon_0 \nabla \cdot \mathbf{E} = \epsilon_0 \sum_{i=1}^3 \nabla_i E_i, \quad (3)$$

The accuracy of the axial electric field measured by MMS is 1 mV/m (ADPs, Ergun et al., 2016), while the accuracy of the components of electric field in the spin plane is < 0.5 mV/m (SDPs, Lindqvist et al., 2016). The two corresponding errors can be denoted as $\delta E_A \sim 1$ mV/m and $\delta E_S \sim 0.5$ mV/m, respectively. It is known that the characteristic spatial scale of MMS is $L \approx 20$ km. Therefore, the error of the charge density calculated from the MMS 4 point electric measurements is estimated to be

$\delta \rho \approx \epsilon_0 \left(\frac{\delta E_A}{L} + 2 \frac{\delta E_S}{L} \right) \approx 0.45$ e/m³ which, as we will see in a case study, is much smaller than the observed charge density. The algorithm presented here is also evaluated and validated by a more sophisticated simulation shown in Figure S1 and S2 in the

supporting information file (jgra55009-sup-0001-2021JA029511-si).

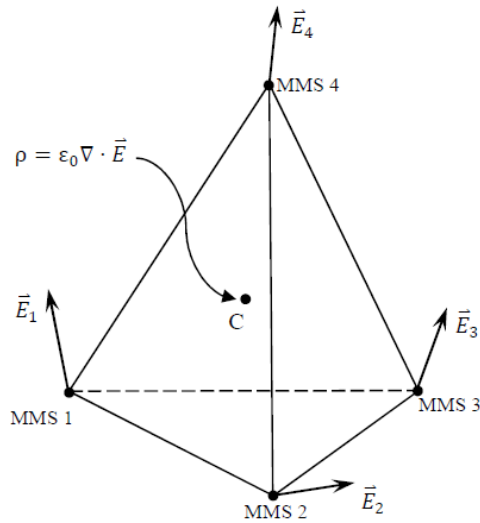


Figure 1. A schematic view of the measurements of the electric field by the MMS constellation and the calculation of the charge density.

Here we will explore the net charge distribution within the magnetopause boundary layer based on MMS electric measurements. It is well known that a charge separation occurs in the magnetopause, brought about by the effects of inertia (because there is a large difference between the masses of the electrons and ions). As a result of that, the net positive charges accumulate at the magnetospheric side and the net negative charges accumulate at the magnetosheath side of the magnetopause boundary. Because the MMS constellation has a rather small size (with the spacecraft separations being several tens of kilometers) and can be well-embedded in the magnetopause boundary, the charge density can be deduced from the MMS electric observations using the above method. We investigate one MMS magnetopause crossing event at 14:26:14 on 11

November 2015 by examining the electric field and calculating the charge density, whose values during the crossing event are shown in Fig. 2. It can be seen that the rotational discontinuity (RD) appear at UT14:26:40 with the maximum magnetic rotation rates (Panel (d)) (Shen et al., 2007), minimum value of the gradient of the magnetic strength (Panel (e)), and smallest radius of curvature of the magnetic field lines (Panel (f)). As shown in Panel (g), a charge separation is evident within the magnetopause boundary, with the positive charges at the magnetospheric side and negative charges at the magnetosheath side. The maximum value of the charge density in the magnetopause is about 60 e/m^3 , which is much larger than the error ($\delta\rho \approx 0.45 \text{ e/m}^3$) as given above. It is evident that the electric neutrality is kept in the magnetosheath near to the magnetopause. These results are in agreement with the conventional kinetic models of the magnetopause boundary layers (Harris, 1962; Lee and Kan, 1979; Parks, 1991; Kivelson and Russell, 1995).

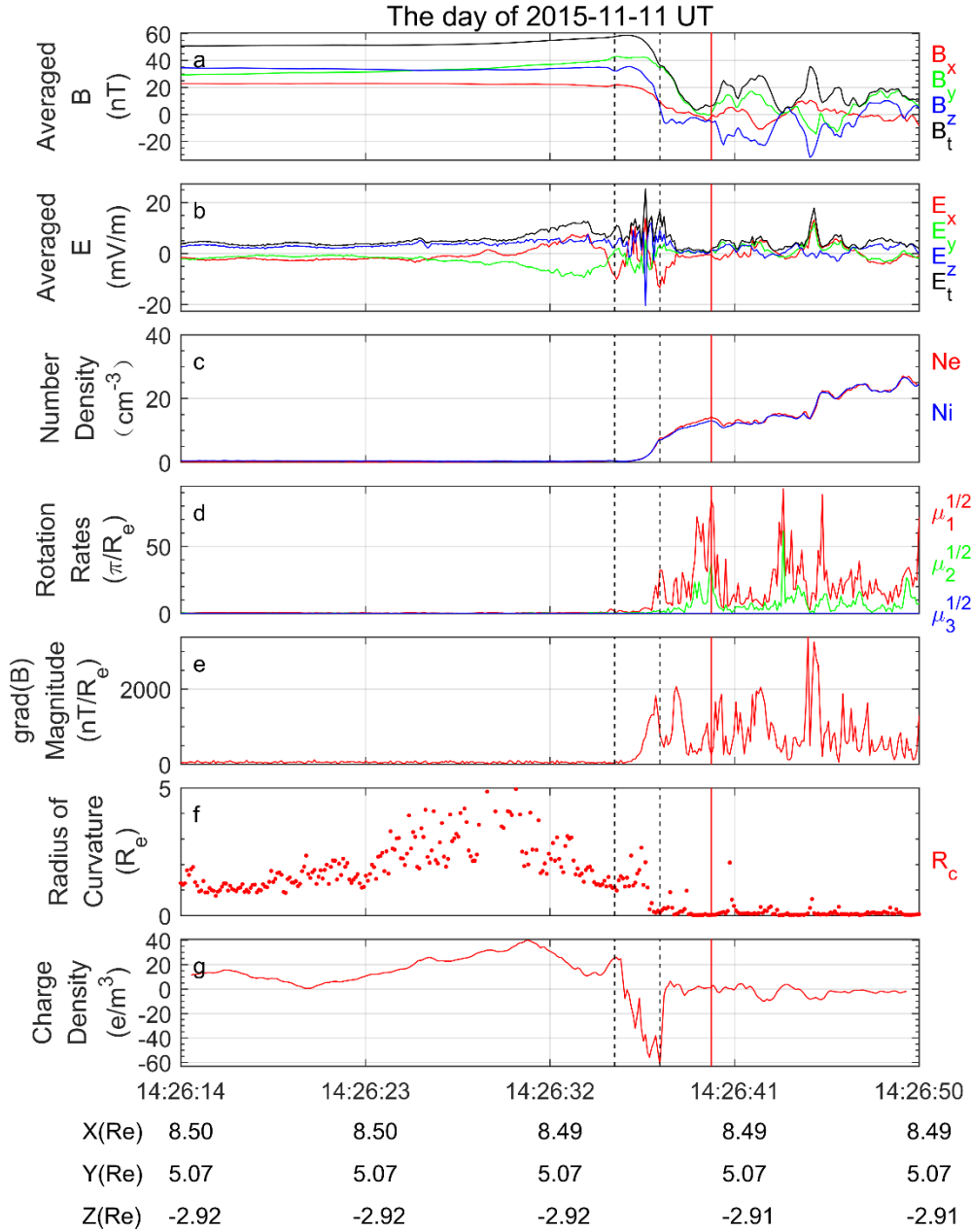


Figure 2. The structure of the magnetopause during an MMS crossing event on 11

November 2015. From top to bottom: (a) the magnetic flux density at the center of the constellation, (b) the electric-field at the center of the constellation, (c) the electron and ion number densities measured by MMS-1 (Pollock et al., 2016), (d) the rotation rates of the magnetic field (Shen et al., 2007), (e) $|\nabla|\mathbf{B}||$, (f) the radius of curvature of the magnetic field lines (Shen et al., 2003), and (g) the charge distribution. The red vertical

line marks the largest rotation rates, and the black vertical dotted lines mark the largest and the smallest charge densities.

3. Charge density measurements from 10 probes on board a spacecraft – Stiff Booms Method

It is known that the linear gradient of a quantity can be estimated based on 4-point measurements (Harvey, 1998; Chanteur, 1998; Shen et al., 2003), while the quadratic gradient of a quantity can be calculated based on 10-point measurements (Chanteur, 1998). In the low Earth Orbit missions DEMETER (Berthelier, et al., 2005) and Zhangheng-1 (Shen, et al., 2018), the electric field is measured with four probes mounted at the ends of four stiff booms. We suggest to construct an electric equipment composed of 10 or more electric probes so that both the electric field and charge density can be measured. In a previous investigation (Shen et al., 2021), a new algorithm was put forward to calculate the linear and quadratic gradients jointly based on 10 or more measurements. It can be applied to obtain the quadratic gradients ($\nabla^2\varphi$) from 10-point electric potential field (φ) measurements. Moreover, with the Poisson equation,

$$\rho = -\varepsilon_0 \nabla^2 \varphi, \quad (4)$$

it yields the distribution of the electric charge density. For the processes with temporal variations, the general governing equation is the d'Alembert equation, $-c^{-2}\partial_t^2\varphi + \nabla^2\varphi = -\varepsilon_0^{-1}\rho$, instead. However, for slow varying structures or steady structures and low-frequency plasma waves with their motion speeds much less than c ,

the first term at the right hand side of the d'Alembert equation can be neglected.

We can check the feasibility of this 10 probe scheme. The electric field generated by a uniformly charged ball will be used to test this approach. Supposing that the radius of the ball is r_0 and its charge density is ρ , we get the electric potential field analytically as,

$$\varphi(\mathbf{r}) = \begin{cases} -\frac{1}{6}\epsilon^{-1}\rho r^2 + \frac{1}{2\epsilon}r_0^2\rho & \text{if } r \leq r_0, \\ -\frac{1}{4\pi\epsilon}\frac{Q}{r} & \text{if } r > r_0, \end{cases} \quad (5)$$

where $Q = \frac{4}{3}\pi r_0^3\rho$ is the total charge and r is the distance from the center of the ball to the measurement point. In the following modeling, constant values of 1 are assigned to ρ , r_0 , and ϵ , i.e., $\rho = r_0 = \epsilon = 1$. The positions of the 10 probes in the barycenter coordinates are generated randomly and presented in Tab. 1 and Fig. 3. The three characteristic lengths of the distribution of the 10 probes (Harvey, 1998; Robert, et al., 1998) are $a = 0.10$, $b = 0.06$, and $c = 0.03$. The reconstructed characteristic matrix \mathfrak{R}^{MN} is

$$(\mathfrak{R}^{MN}) = \begin{pmatrix} 12.73 & -11.09 & -5.05 & 5.22 & 2.74 & 1.61 \\ -11.09 & 20.90 & 5.47 & -6.71 & -4.97 & -2.28 \\ -5.05 & 5.47 & 6.44 & -2.49 & -4.56 & -2.27 \\ 5.22 & -6.71 & -2.49 & 12.83 & -1.91 & 2.27 \\ 2.74 & -4.97 & -4.56 & -1.91 & 9.09 & 0.86 \\ 1.61 & -2.28 & -2.27 & 2.27 & 0.86 & 2.68 \end{pmatrix} 10^{-3}, \quad (6)$$

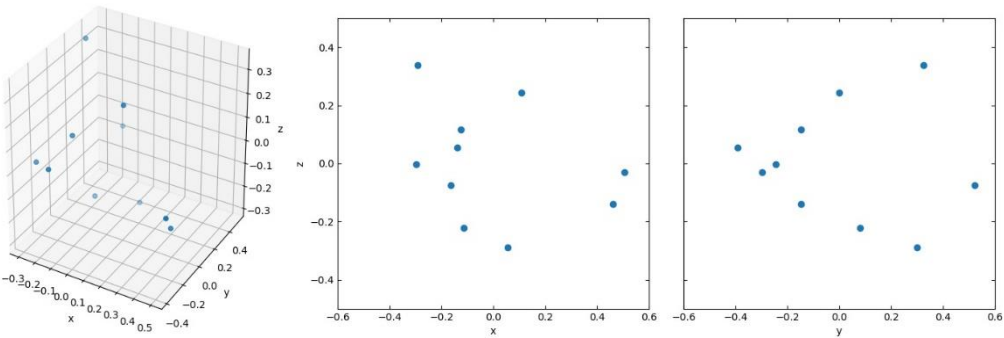
and its eigenvalues are given in Tab. 2.

259

260

Table 1. The locations of the 10 probes in the barycenter coordinates .

x	y	z
-0.16474	0.520923	-0.07516
-0.29774	-0.2433	-0.00151
0.107263	-0.00029	0.243785
-0.12458	-0.14707	0.116693
-0.11324	0.080113	-0.22108
0.505285	-0.29726	-0.0293
0.055479	0.300437	-0.28976
0.461577	-0.14647	-0.13865
-0.2916	0.323618	0.339179
-0.13771	-0.3907	0.055801



261

262

Figure 3. The distribution of the 10 probes.

263

264

Table 2. The eigenvalues of the characteristic matrix \mathfrak{R}^{MN} .

0.03614	0.01326	0.00114	0.00235	0.00510	0.00668
---------	---------	---------	---------	---------	---------

We first investigate the behavior of the resultants with the number of iterations.

D is the local characteristic scale of the electric field structure and is set equal to r in this model. It is assumed that the barycenter of the constellation is at $[0.1,0,0]$, and the probe separations L are reduced proportionally so that the relative measurement scale $L/D = 0.026$. The relative truncation error, $X_{algorithm}/X_{real} - 1$, is shown in Fig. 4.

With increasing numbers of iterations, the errors decrease and finally converge to certain fixed values. In this calculation, the solution converges after 100 iterations. By testing various fields, we found that the number of iterations required for convergence varies.

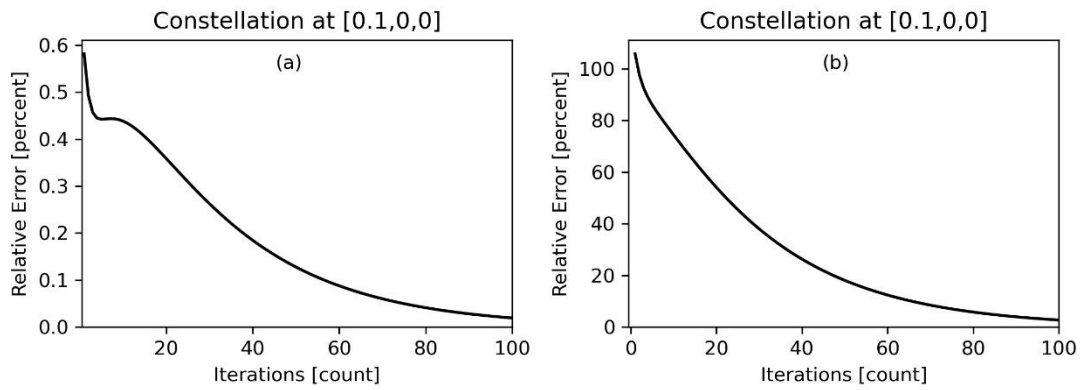


Figure 4. The relative errors of the linear (a) and the quadratic (b) electric potential gradients, i.e., $\partial_x \phi$ and $\partial_x \partial_x \phi$, calculated for different numbers of iterations at $[0.1,0,0]$ within the uniformly charged ball.

282

283 Secondly, we investigate the dependence of the truncation errors on the relative
284 measurement scale L/D . We have tested six situations, with the barycenter of the 10
285 probes located at three representative points within the ball, $[0.1,0,0]$, $[0.4,0,0]$, and
286 $[0.7,0,0]$, and three points outside the ball, $[3,0,0]$, $[5,0,0]$, and $[8,0,0]$. We scale up
287 and down the size of the original 10 probes to adjust the characteristic size L and
288 therefore L/D .

289

290 Figure 5 shows the errors modeled in the ball. In general, the errors are less than
291 $10^{-5}\%$ for the linear gradients and less than 0.02% for the quadratic gradients. With
292 the same number of iterations, 1000, the errors at different positions vary by an order
293 of 2. The extremely accurate results arise from the fact that the charge density has been
294 assume homogeneous and electric field is linear varying within the charged ball. A
295 further check on the method for a charged ball model with a non-uniform charge density
296 ball has been performed in the Supporting Information file (jgra55009-sup-0002-
297 2021JA029511-si).

298

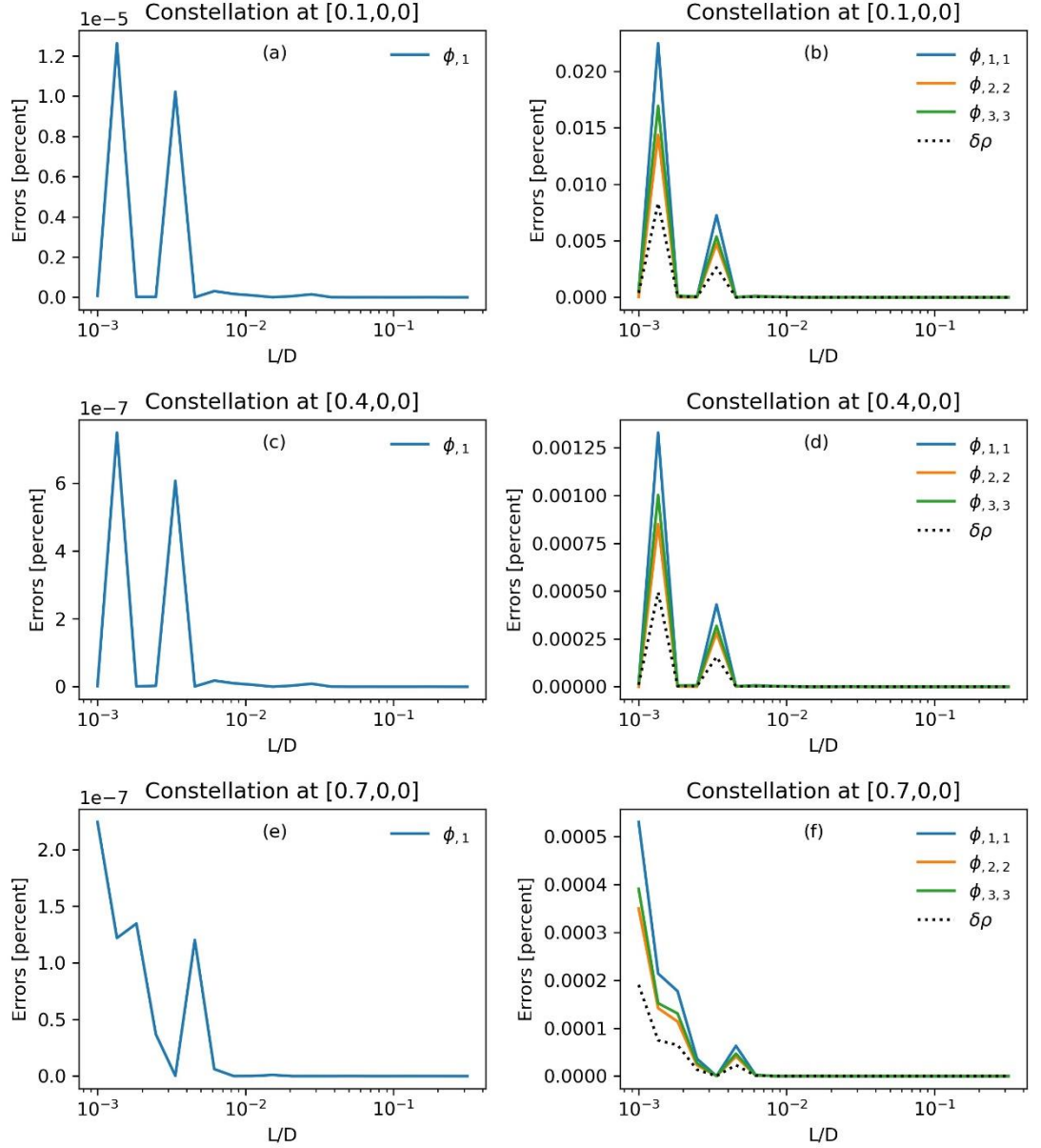


Figure 5. The variation of the errors of the calculation by using the 10-probe scheme with the relative measurement scale L/D for the case of a uniformly charged ball. The measurements are performed inside of the charged ball. The left panels, (a), (c), and (e), show the truncation errors for the non-vanishing component of the linear gradient by L/D calculated for three different locations of the barycenter of the 10 probes inside the ball, $[0.1,0,0]$, $[0.4,0,0]$, and $[0.7,0,0]$. The right panels, (b), (d), and (f), illustrate the relative errors of the non-vanishing components of the quadratic gradient

and charge density (dashed line) calculated for the same three locations of the barycenter. It is noted that $\phi_{,1} \equiv \partial_x \phi$ and $\phi_{,2,2} \equiv \partial_y \partial_y \phi$, where a comma denotes partial differentiation.

Figure 6 shows the modeling results outside of the ball. As $L/D < 0.01$, the relative errors of the non-vanishing quadratic gradient components are below 2%. The attained linear and quadratic gradients are accurate to second order and first order, respectively.

The same error analysis procedure for the 10-probe scheme has been applied to another charged ball model in which the charge density is inversely proportional to the square of the distance from the ball center, as shown in Figure S3 and S4 in the Supporting Information file (jgra55009-sup-0002-2021JA029511-si), and a similar conclusion has been reached.

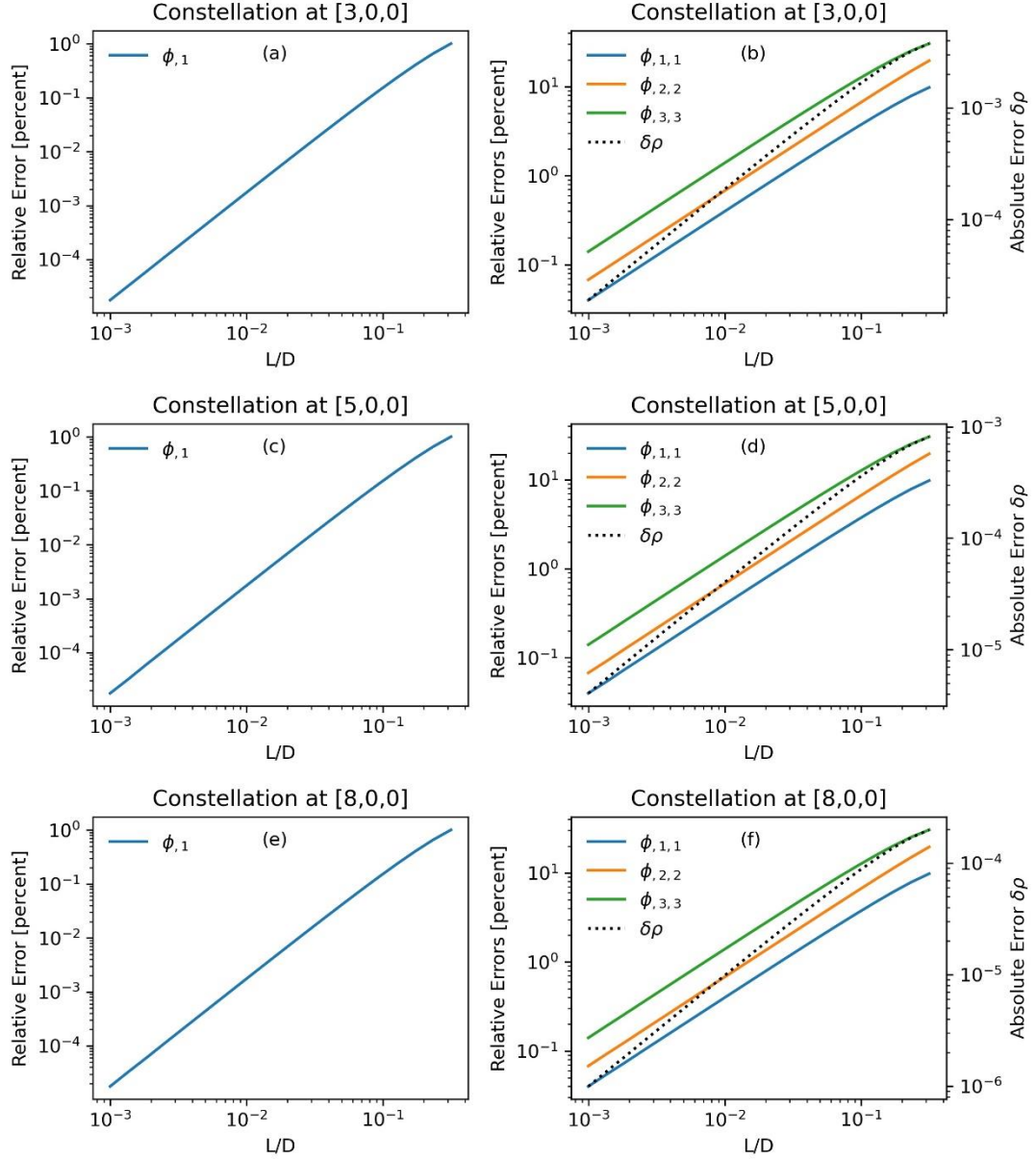


Figure 6. The dependence of the truncation errors of the calculations by using the 10-probe scheme on the relative measurement scale L/D for the case of a uniformly charged ball. The measurements are performed outside of the charged ball. The left panels, (a), (c), and (e), show the truncation error for the non-vanishing component of the linear gradient as a function of L/D calculated for three different locations of the barycenter of the 10 probes outside of the ball, [3,0,0], [5,0,0], and [8,0,0]. The right panels, (b), (d), and (f), illustrate the relative errors of the non-vanishing components of the

quadratic gradient and the absolute value of the charge density (dashed line) calculated for the same three locations of the barycenter. It is noted that the real charge density outside of the ball is zero.

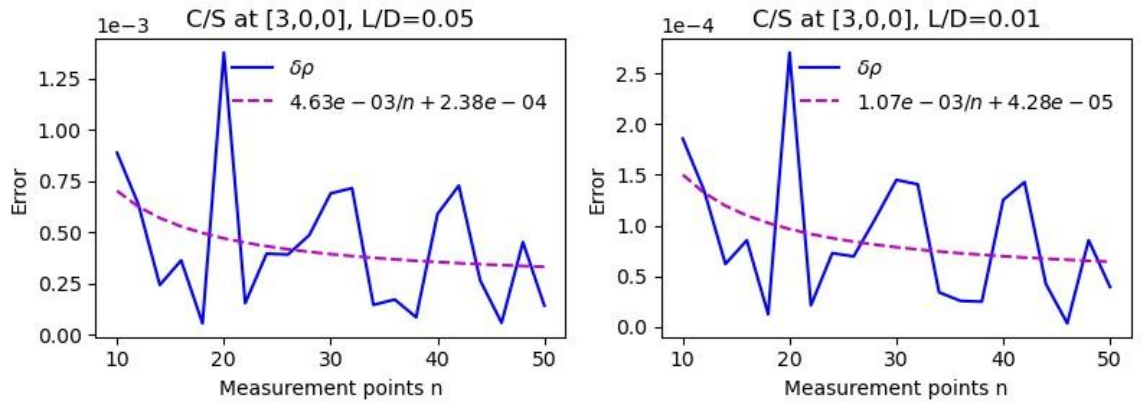


Figure 7. The relation between the absolute error of the charge density and the number of measurement points at $[3,0,0]$. The relative measurement scale is chosen as $L/D = 0.05$ (left) and $L/D = 0.01$ (right). The dashed lines are fitted from the modeled errors.

We further investigate the relationship between the accuracy of the density estimated and the number of the probes used. Figure 7 indicates that the accuracy of the charge density is not improved significantly as the number of probes is increased. Therefore, 10 probes with a proper spatial configuration will be sufficient for robust measurements of the charge density.

This scheme is possible to be used for the net charge measurements on the low Earth orbits at the altitudes of several hundred kms, for which the 10 probes are mounted at the ends of 10 booms with different lengths, and the spacecraft can be either

348 spinning or not.

349 The feasibility of the measurements at the low attitude Earth orbits can be shown
350 by including observational errors. The accuracy of the probes is assumed at
351 $\delta\phi \approx L\delta\nabla\phi \sim 10m \times 0.5mV/m \sim 5mV$. The electric potential at an arbitrary probe can
352 be expanded as the following.

$$\begin{aligned}\phi &= \phi_c + \Delta\mathbf{x} \cdot \nabla\phi + \frac{1}{2} \Delta\mathbf{x} \Delta\mathbf{x} \cdot \nabla\nabla\phi \\ &\sim \phi_c - E \cdot L + \frac{1}{2} \frac{1}{\epsilon_0} \rho L^2,\end{aligned}$$

354 where, $\Delta\mathbf{x}$ is the distance of the probe from the center, which is at the scale of L ;
355 $\nabla\phi = -\mathbf{E}$, and $\nabla\nabla\phi$ is estimated by $\nabla^2\phi = -\rho/\epsilon_0$. The second term at the right
356 hand side (or the first order term) is the contribution of the electric field, which is about
357 $EL \sim 600mV/m \times 10m \sim 6.0V$. The third term (or the second order term) is the
358 contribution of the charge density, which is about $\frac{1}{2} \frac{1}{\epsilon_0} \rho L^2 \sim 50mV$ if the typical
359 value of the charge density at low Earth orbits is assumed to be $\rho \sim 5 \times 10^4 e/m^3$, which
360 is about three order higher than those at the high Earth orbits. They are both much larger
361 than the probe sensitivity ($5mV$), so that at low Earth orbits the charge density is
362 observable with the approach described above.

364 4. Measuring the charge density with seven or eight electric potential probes

365 Only three diagonal components of the quadratic gradient of the electric potential
366 are contained in the Poisson equation ($\rho \propto \nabla^2\phi = \partial^2/\partial x^2\phi + \partial^2/\partial y^2\phi + \partial^2/\partial z^2\phi$). The
367 three other cross-components of the quadratic gradient, $\partial_x\partial_y\phi$, $\partial_y\partial_z\phi$, and $\partial_z\partial_x\phi$,

are of no use for computing the charge density, so three independent parameters can be neglected in this algorithm. Therefore, $10-3=7$ probes are sufficient to acquire the data for the estimation of the Laplacian operator on the electric potential ($\nabla^2\phi$) as well as the charge density.

4.1 Seven-probe scheme

A seven-probe scheme, which is similar to the electric potential measurement of the MMS at high altitude orbits, is shown in Fig. 8. All probes are placed on three axes of the Cartesian coordinate system. The spatial parameters are $x_2=-x_1=L_x$, $y_2=-y_1=L_y$, and $z_2=-z_1=L_z$. By taking differences, the linear and quadratic gradients at second-order accuracy can be obtained to estimate the charge density at the center.

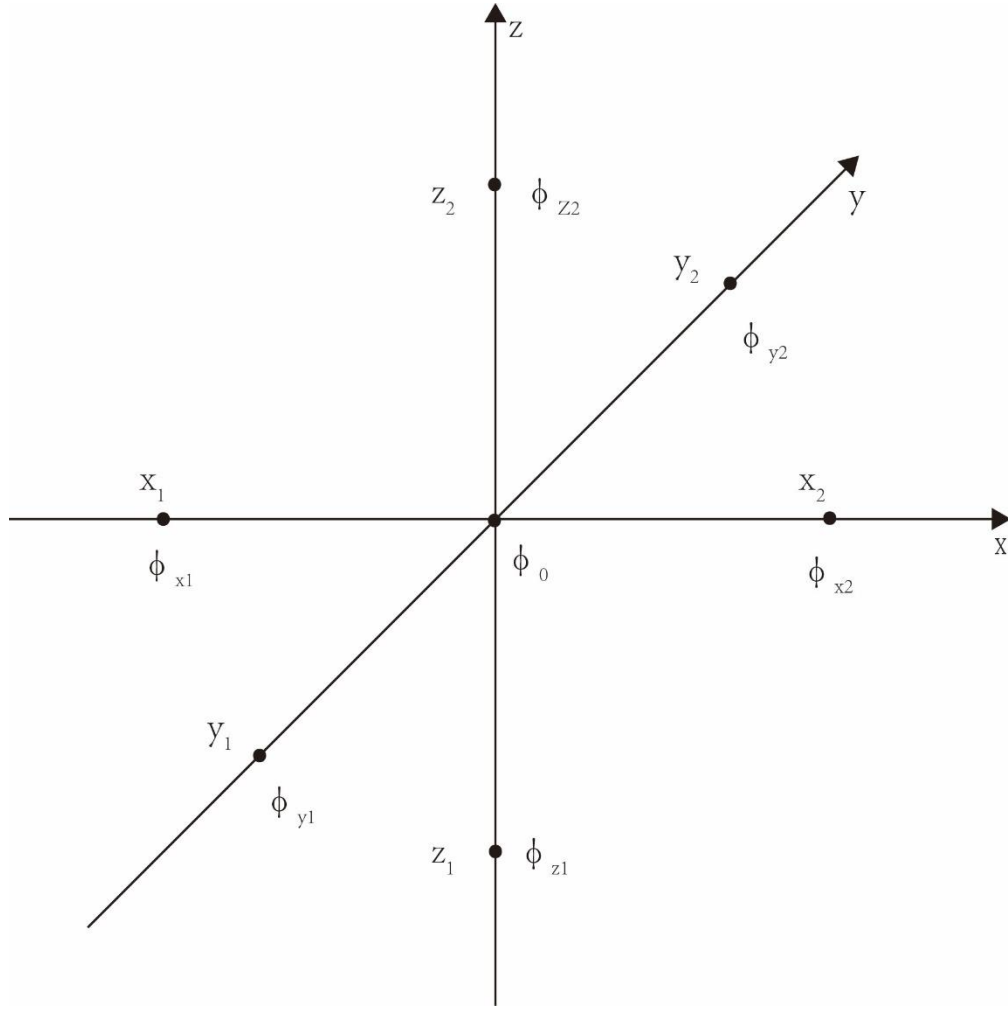


Figure 8. A schematic view of the seven-probe measurement of the charge density. The probes are indicated by black dots.

The linear and quadratic gradients along the x-axis are

$$\left\{ \begin{array}{l} \partial_x \phi = \frac{\phi_{x2} - \phi_{x1}}{2L_x} \end{array} \right. \quad (7)$$

$$\left\{ \begin{array}{l} \partial_x^2 \phi = \frac{\phi_{x2} - \phi_0}{L_x} - \frac{\phi_0 - \phi_{x1}}{L_x} = \frac{(\phi_{x2} + \phi_{x1}) - 2\phi_0}{L_x^2} \end{array} \right. \quad (8)$$

Similarly, the linear and quadratic gradients along the y-axis are

$$\begin{cases} \partial_y \phi = \frac{\phi_{y2} - \phi_{y1}}{2L_y} & (9) \\ \partial_y^2 \phi = \frac{(\phi_{y2} + \phi_{y1}) - 2\phi_0}{L_y^2} & (10) \end{cases}$$

The linear and quadratic gradients along the z-axis are

$$\begin{cases} \partial_z \phi = \frac{\phi_{z2} - \phi_{z1}}{2L_z} & (11) \\ \partial_z^2 \phi = \frac{(\phi_{z2} + \phi_{z1}) - 2\phi_0}{L_z^2} & (12) \end{cases}$$

The linear and quadratic gradients are both accurate to second order.

However, in actual measurements, the central probe is inside the spacecraft and cannot determine the electric potential accurately. To improve this measurement, the central probe is replaced by another two additional probes located on the z-axis. The algorithm for this is shown in the following section. It is noted the seven-probe scheme can be still applied to the electric field and charge density measurements in ground-based laboratory experiments.

4.2 Eight-probe scheme

The eight-probe scheme is shown in Fig. 9 with $x_2 = -x_1 = L_x$, $y_2 = -y_1 = L_y$, $z_3 = -z_2 = L_z$, and $z_4 = -z_1 = L_z + l_z$. The algorithm is constructed as follows.

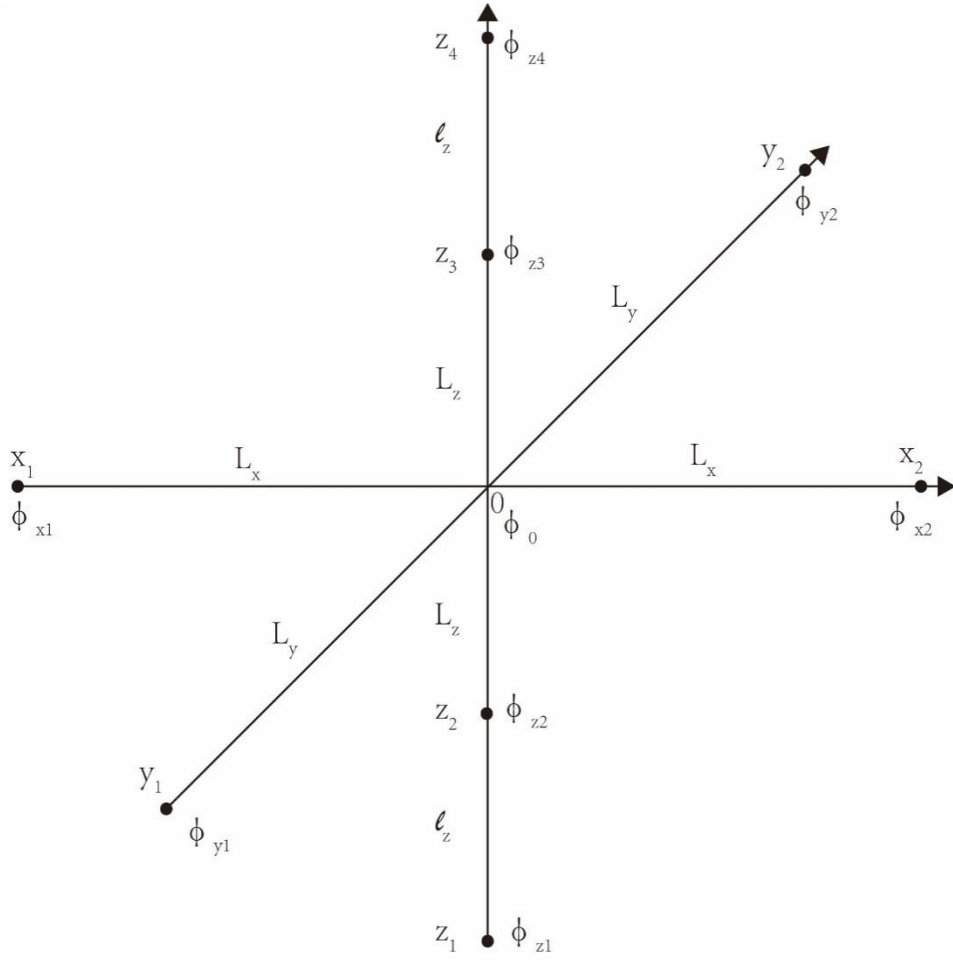


Figure 9. A schematic view of the eight-probe measurement of charge density.

The four electric potentials observed by the probes on the z-axis can be expressed as a

Taylor series. By keeping the first five terms we get

$$\phi_{z1} = \phi_0 + z_1 \partial_z \phi + \frac{1}{2} z_1^2 \partial_z^2 \phi + \frac{1}{3!} z_1^3 \partial_z^3 \phi + \frac{1}{4!} z_1^4 \partial_z^4 \phi \quad (13)$$

$$\phi_{z2} = \phi_0 + z_2 \partial_z \phi + \frac{1}{2} z_2^2 \partial_z^2 \phi + \frac{1}{3!} z_2^3 \partial_z^3 \phi + \frac{1}{4!} z_2^4 \partial_z^4 \phi \quad (14)$$

$$\phi_{z3} = \phi_0 + z_3 \partial_z \phi + \frac{1}{2} z_3^2 \partial_z^2 \phi + \frac{1}{3!} z_3^3 \partial_z^3 \phi + \frac{1}{4!} z_3^4 \partial_z^4 \phi \quad (15)$$

$$\phi_{z4} = \phi_0 + z_4 \partial_z \phi + \frac{1}{2} z_4^2 \partial_z^2 \phi + \frac{1}{3!} z_4^3 \partial_z^3 \phi + \frac{1}{4!} z_4^4 \partial_z^4 \phi \quad (16)$$

412 Summing up the above four equations leads to

$$413 \quad (\phi_{z1} + \phi_{z2} + \phi_{z3} + \phi_{z4}) = 4\phi_0 + \frac{1}{2}(z_1^2 + z_2^2 + z_3^2 + z_4^2)\partial_z^2\phi + \frac{1}{4!}(z_1^4 + z_2^4 + z_3^4 + z_4^4)\partial_z^4\phi \quad .$$

414 The electric potential at the center is therefore

$$415 \quad \phi_0 = \frac{1}{4}(\phi_{z1} + \phi_{z2} + \phi_{z3} + \phi_{z4}) - \frac{1}{8}(z_1^2 + z_2^2 + z_3^2 + z_4^2)\partial_z^2\phi - \frac{1}{96}(z_1^4 + z_2^4 + z_3^4 + z_4^4)\partial_z^4\phi \quad (17)$$

416 Subtracting Eq. (13) from Eq. (16) and Eq. (14) from Eq. (15) gives

$$417 \quad \begin{cases} \phi_{z4} - \phi_{z1} = (z_4 - z_1) \partial_z\phi + \frac{1}{3!}(z_4^3 - z_1^3)\partial_z^3\phi \\ \phi_{z3} - \phi_{z2} = (z_3 - z_2) \partial_z\phi + \frac{1}{3!}(z_3^3 - z_2^3)\partial_z^3\phi \end{cases} \quad (18)$$

418 or

$$419 \quad \begin{cases} \phi_{z4} - \phi_{z1} = 2z_4\partial_z\phi + \frac{1}{3}z_4^3\partial_z^3\phi \\ \phi_{z3} - \phi_{z2} = 2z_3\partial_z\phi + \frac{1}{3}z_3^3\partial_z^3\phi \end{cases} \quad (18')$$

420 Then, we get the linear gradient along the z-axis at the center as

$$421 \quad \partial_z\phi = \frac{z_3^3(\phi_{z4} - \phi_{z1}) - z_4^3(\phi_{z3} - \phi_{z2})}{2z_4z_3^3 - 2z_3z_4^3} \quad (19)$$

422 The expression above is of fourth-order accuracy. On the other hand, from Equation

423 (18), the third-order derivative of electric potential along the z-axis is

$$424 \quad \partial_z^3\phi = \frac{3z_3(\phi_{z4} - \phi_{z1}) - 3z_4(\phi_{z3} - \phi_{z2})}{z_3z_4^3 - z_4z_3^3} \quad (20)$$

425 The expression above is of second-order accuracy.

426 Subtracting the sum of Eq. (14) and Eq. (15) from the sum of Eq. (13) and Eq. (16), we

427 get

$$428 \quad (\phi_{z4} + \phi_{z1}) - (\phi_{z3} + \phi_{z2}) = \frac{1}{2}(z_1^2 + z_4^2 - z_2^2 - z_3^2)\partial_z^2\phi + \frac{1}{4!}(z_1^4 + z_4^4 - z_2^4 - z_3^4)\partial_z^4\phi$$

429 The second-order derivative is, therefore,

$$430 \quad \partial_z^2 \phi = \frac{2(\phi_{z4} + \phi_{z1} - \phi_{z3} - \phi_{z2})}{(z_1^2 + z_4^2 - z_2^2 - z_3^2)} - \frac{1}{12} \frac{(z_1^4 + z_4^4 - z_2^4 - z_3^4)}{z_1^2 + z_4^2 - z_2^2 - z_3^2} \partial_z^4 \phi \quad (21)$$

431 The expression above is of second-order accuracy.

432 Substituting Eq. (21) into Eq. (17), we get the corrected potential ϕ_0 at the center
433 as

$$434 \quad \phi_0 = \frac{1}{4}(\phi_{z1} + \phi_{z2} + \phi_{z3} + \phi_{z4}) - \frac{1}{4} \frac{z_1^2 + z_2^2}{z_1^2 - z_2^2} (\phi_{z4} + \phi_{z1} - \phi_{z3} - \phi_{z2}) + \frac{1}{24} z_1^2 z_2^2 \partial_z^4 \phi \quad (17')$$

435 The above expression is of fourth-order accuracy because the expression is
436 truncated at the fourth-order term.

437 Furthermore, by neglecting high order terms, we get the estimators for the
438 potential and its linear and quadratic gradients at the center as

$$\begin{cases} \partial_z^2 \phi = \frac{(\phi_{z4} + \phi_{z1}) - (\phi_{z3} + \phi_{z2})}{l_z(2L_z + l_z)} & (21') \\ \partial_z \phi = \frac{(L_z + l_z)^3(\phi_{z3} - \phi_{z2}) - L_z^3(\phi_{z4} - \phi_{z1})}{2L_z(L_z + l_z)(2l_z L_z + l_z^2)} & (19') \\ \phi_0 = \frac{1}{4}(\phi_{z1} + \phi_{z2} + \phi_{z3} + \phi_{z4}) - \frac{(L_z + l_z)^2 + L_z^2}{4l_z(2L_z + l_z)} (\phi_{z4} + \phi_{z1} - \phi_{z3} - \phi_{z2}) & (17'') \end{cases}$$

440 As stated above, the second-order derivative along the z-axis is of second-order
441 accuracy. The potential and its first-order derivative along the z-axis are of fourth-order
442 accuracy.

443 Similar to the seven-probe scheme, the first-order and second-order derivatives of
444 the potential along the x- and y-axis are subjected to Eqs. (7)-(10). The central potential
445 ϕ_0 is calculated with Eq. (17''). The first-order and second-order derivatives along the
446 x- and y-axis are of second order accuracy.

The electric field at the center is

$$\mathbf{E} = -\hat{\mathbf{e}}_x \partial_x \phi - \hat{\mathbf{e}}_y \partial_y \phi - \hat{\mathbf{e}}_z \partial_z \phi \quad (22)$$

Using the Poisson equation (4), the charge density is obtained as

$$\begin{aligned} \rho &= -\epsilon_0 (\partial_x^2 \phi + \partial_y^2 \phi + \partial_z^2 \phi) \\ &= -\epsilon_0 \left[\frac{(\phi_{x2} + \phi_{x1}) - 2\phi_0}{L_x^2} + \frac{(\phi_{y2} + \phi_{y1}) - 2\phi_0}{L_y^2} + \frac{(\phi_{z4} + \phi_{z1}) - (\phi_{z3} + \phi_{z2})}{l_z(2L_z + l_z)} \right] \end{aligned} \quad (23)$$

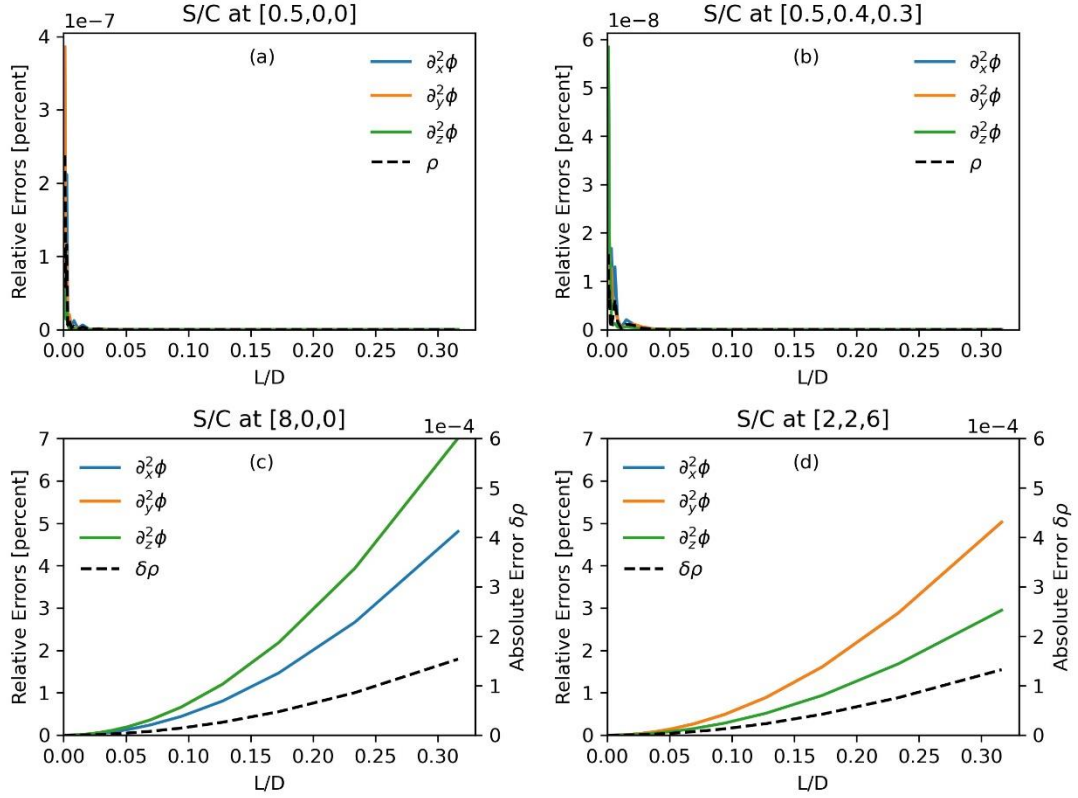
where ϕ_0 is given by Eq. (17”).

The eight-probe scheme will now be examined for the electric field produced by a uniformly-charged ball.

The relationship between the relative truncation errors and the relative measurement scale, L/D , is studied when we set $L_x = L_y = L_z = l_z$ and scale up and down the distances between the spacecraft to adjust L/D . Due to the broken spherical symmetry, two points inside the ball, $[0.5, 0, 0]$ and $[0.5, 0.4, 0.3]$, and two points outside of the ball, $[8, 0, 0]$ and $[2, 2, 6]$, are chosen as the representative points. The modeled results are shown in Fig. 10. The quadratic gradient in the ball is close to a constant and the charge density here is a constant. The truncation errors given by the algorithm, as shown in Fig. 10 (a,b), are negligible in this case. The charge density outside the ball is zero, and the calculated density, amounting to 10^{-4} as shown by the dashed lines in Fig 10 (c,d), is fairly close to zero. Note that the scale is one in the modeled system. As $L/D < 0.1$, the truncation errors of the quadratic gradient are less than 2%. It can be seen that the relative errors of the quadratic gradient and hence the charge density are at second order in L/D .

468

469



470

471 **Figure 10.** The dependence of the truncation errors of the calculations by using the 8-
 472 probe scheme on the relative measurement scale L/D for the case of a uniformly charged
 473 ball. Panel (a) and (b) show the relative truncation errors of the quadratic gradient of
 474 the electric potential (solid lines) and the charge density (dashed lines) at $[0.5,0,0]$ and
 475 $[0.5,0.4,0.3]$ in the ball, respectively. Panel (c) and (d) show the relative truncation
 476 errors of the quadratic gradient of the electric potential (solid lines and left vertical axis)
 477 and the absolute errors of the charge density (dashed lines and right vertical axis) at
 478 $[8,0,0]$ and $[2,2,6]$ out of the ball. In panel (c), the orange line orange line is overlaid
 479 with the green line. In panel (d), the blue line is overlaid with the orange line.

480

For real measurements in space, the distances between the probes along the z-axis, L_z and l_z , are much smaller than those along the other axes, L_x and L_y . The truncation error in real case, therefore, should be less than evaluated when setting them all equal.

An error analysis on the eight-probe scheme using the charged ball model of $\rho = b/r^2$ is also conducted. The result as shown in Figure S5 in Supporting Information (jgra55009-sup-0002-2021JA029511-si) has further confirmed the accuracy of this algorithm. This 8 probe scheme is potentially applied for the net charge measurements on the high altitude orbits, for which the spacecraft is spinning thus that the four probes can stretch out at the ends of the four wire booms on the spin plane as shown in Fig. 9. Performing similar error analysis as in Section 3, it is found the sensitivity of the probes is required to reach 0.5mV, which still need technical efforts to achieve in the future.

5. Summary and Discussions

Preliminary explorations for measuring the net charge density in space have been presented in this paper. Three schemes for the charge density measurements have been developed.

The first scheme deduces the charge density based on four spacecraft electric field measurements. Based on the electric fields (\mathbf{E}_α , $\alpha = 1,2,3,4$) observed at the four spacecraft, we can obtain the gradient of the electric field at the barycenter of the constellation, $(\nabla \mathbf{E})_c$, and furthermore, the divergence of the electric field, $(\nabla \cdot \mathbf{E})_c$. The Gaussian theorem yields the charge density as $\rho = \epsilon \nabla \cdot \mathbf{E}$. This algorithm requires

the constellation not to be distributed in a plane or linearly. In other words, the three eigenvalues of the volumetric tensor of the constellation should be non-vanishing. Based on this algorithm, an analysis on the electric field data acquired during a dayside magnetopause crossing event by the MMS constellation shows a charge separation in the magnetopause boundary layer and that the positive charges are accumulated on the magnetospheric side while the negative charges are accumulated on the magnetosheath side. A normal electric field pointing at the magnetosheath is also discovered. This confirms a previous theoretical prediction (Parks, 1991; Kivelson and Russell, 1995).

Another charge density measurement scheme is based on 10 or more electric potential probes. By using a newly-developed algorithm [Shen et al., 2021], the linear gradient, $(\nabla\phi)_c$, and the quadratic gradient, $(\nabla\nabla\phi)_c$, of the electric potential at the center of the probes can be calculated from the $N \geq 10$ electric potentials, $\phi_\alpha (\alpha = 1, 2, \dots, N)$, as measured at the N probes. Furthermore, the electric field and the net charge density at the center of the probes can be calculated using $\mathbf{E} = -(\nabla\phi)_c$ and the Poisson equation, $\rho = -\epsilon\nabla^2\phi$, respectively.

This scheme requires the probes to be distributed uniformly. In other words, the eigenvalues of the 6×6 matrix \mathfrak{R} should be non-vanishing (Shen et al., 2021). The accuracy of the charge density estimated by the algorithm is of first order and that of the electric field is of second order. Modeling also shows that more probes lead to higher accuracy.

Finally, two other schemes are presented to measure the electric charge density, which improve on the existing schemes for electric field observations onboard spacecraft. If one more electric potential probe is added in addition to the six electric potential probes of the electric field equipment on board the MMS spacecraft (that are distributed symmetrically on the three axes of the Cartesian coordinate system), the charge density can be derived along with the electric field vectors. The seventh probe is placed at the origin of the coordinate system. Due to the shielding potential of the spacecraft, this seven-probe scheme cannot be applied to measurements in space. However, it can be utilized in charge density measurements in ground-based laboratory experiments. Alternatively, by placing two more probes symmetrically on the two stiff booms in the six-point scheme of the MMS constellation, the eight-probe scheme will work for charge density measurements in space. The simulation test shows that the estimated electric field is of fourth-order accuracy and the charge density is of second-order accuracy. The truncation errors contained in this scheme are much less than those in the 10 -probe scheme. The implementation of this scheme requires further development in the future.

Acknowledgments

This work was supported by National Natural Science Foundation (NSFC) of China (Grant No. 41874190) and the Shenzhen Technology Project (JCYJ20190806144013077). The MMS data were obtained from the MMS Science Data Center (<http://lasp.colorado.edu/mms/sdc/>). We thank the MMS plasmas and field teams for providing with these high quality data.

References

- Akasofu, S.-I. (1981), The aurora: An electrical discharge phenomenon surrounding the Earth. *Rep. Prog. Phys.*, 44, 1123.
- Argall, M., Shuster, J., Dors, I., Genestreti, K., Nakamura, T., Torbert, R., et al. (2019). How neutral is quasi-neutral: Charge Density in the Reconnection Diffusion Region Observed by MMS. *Earth and Space Science Open Archive*, 1. <https://doi.org/10.1002/essoar.10501410.1>
- Alfvén, H. (1963), *Cosmical Electrodynamics: Fundamental Principles*, by Hannes Alfvén and Carl-Gunne Fälthammar., p. 158-159, Clarendon Press.
- Axford, W. I. (1968). The polar wind and the terrestrial helium budget. *J. Geophys. Res.*, 73, 6855.
- Berthelier, J. J., M. Godefroy, F. Leblanc, M. Malingre, M. Menvielle, et al. (2005), ICE, the electric field experiment on DEMETER. *Planetary and Space Science*, 54(5), 456–471. <https://doi.org/10.1016/j.pss.2005.10.016>
- Bittencourt, J. A. (2004), *Fundamentals of plasma physics*, p. 256. Springer.
- Block, L. (1975), Double layers, in *Physics of the Hot Plasma in the Magnetosphere*, edited by B. Hultqvist and L. Stenflo, p. 229, Springer, New York.
- Burch, J. L., Moore, T. E., Torbert, R. B., and Giles, B. L. (2016), Magnetospheric Multiscale overview and science objectives. *Space Science Reviews*, 199(1-4), 5–21. <https://doi.org/10.1007/s11214-015-0164-9>.

591 Chanteur, G. (1998), Spatial Interpolation for four spacecraft: Theory, in *Analysis*
 592 *Methods for Multi-Spacecraft Data*, edited by G. Paschmann and P. W. Daly, p. 349,
 593 ESA Publ. Div., Noordwijk, Netherlands.

594 Escoubet, C. P., Fehringer, M., & Goldstein, M. (2001), Introduction: The Cluster
 595 mission, *Annales Geophysicae*, 19, 1197-1200, [https://doi.org/10.5194/angeo-19-](https://doi.org/10.5194/angeo-19-197-2001)
 596 [197-2001](https://doi.org/10.5194/angeo-19-197-2001).

597 Haaland, S., Hasegawa, H., Paschmann, G., Sonnerup, B., & Dunlop, M. (2021).
 598 20 years of Cluster observations: The magnetopause. *Journal of Geophysical*
 599 *Research: Space Physics*, 126, e2021JA029362. [https://doi.](https://doi.org/10.1029/2021JA029362)
 600 [org/10.1029/2021JA029362](https://doi.org/10.1029/2021JA029362)

601 Harvey, C. C. (1998), Spatial gradients and the volumetric tensor, in *Analysis Methods*
 602 *for Multi-Spacecraft Data*, edited by G. Paschmann and P. W. Daly, p. 307, ESA
 603 Publications Division, Noordwijk, The Netherlands.

604 Harris, E.G.(1962). On a plasma sheath separating regions of oppositely directed
 605 magnetic field. *Nuovo Cim* 23, 115–121 . <https://doi.org/10.1007/BF02733547>.

606 Hasegawa, A. and I. Sato (1989), *Space Plasma Physics, I Stationary Processes*, p. 153-
 607 156, Springer-Verlag, Berlin, Heidelberg, Germany.

608 Lee, L. C. , and Kan, J. R. (1979). A unified kinetic model of the tangential
 609 magnetopause structure. *Journal of Geophysical Research Space Physics*, 84(A11),
 610 6417-6426.

611 Lemaire, J., and V. Pierrard (2001), Kinetic Models of Solar and Polar Winds.
 612 *Astrophysics and Space Science*, 277, 169–180.

613 Michael, C. K. (2014), *The Earth's Electric Field: Sources From Sun to Mud*, p. 66, 168,
614 204, Elsevier, 225 Wyman Street, Waltham, MA 02451, USA.

615 Mozer F. S., and Bruston, P. (1967), Motion of artificial ion clouds in upper atmosphere.
616 *Journal of Geophysical Research*, 72, 1109-1114.

617 Mozer, F. S. (1973), Analyses of techniques for measuring dc and ac electric fields in
618 the magnetosphere. *Space Sci. Rev.*, 14, 272-313.

619 Parks, G. K. (1991), *Physics Of Space Plasmas: An Introduction*, p. 355-369, Redwood
620 City, CA, Addison-Wesley Publishing Co..

621 Paschmann G., F. Melzner, R. Frenzel, et al. (1997), The electron drift instrument for
622 Cluster[J]. *Space Science Reviews*, 79, 233-269.

623 Paschmann, G., Haaland, S., Sonnerup, B. U. O., Hasegawa, H., Georgescu, E., Klecker,
624 B., et al. (2005). Characteristics of the near-tail dawn magnetopause and boundary
625 layer. *Annales de Geophysique*, 23(4), 1481–1497. [https://doi.org/10.5194/angeo-](https://doi.org/10.5194/angeo-23-1481-2005)
626 23-1481-2005

627 Pedersen A. F., Mozer F. S., and Gustafsson G. (1998), Electric field measurements in a
628 tenuous plasma with spherical double probes, in *Measurement Techniques in Space*
629 *Plasmas – Fields*, edited by R. F. Pfaff, J. E. Borovsky, and D. T. Young, p. 1-12,
630 AGU Geophysical Monograph 103, AGU, Washington DC.

631 Pollock, C., Moore, T. E., Jacques, A., Burch, J., Gliese, U., Saito, Y., et al. (2016), Fast
632 plasma investigation for Magnetospheric Multiscale. *Space Science Reviews*,
633 199(1-4), 331–406. <https://doi.org/10.1007/s11214-016-0245-4>.

634 Raadu, M. A. (1989), The physics of double layers and their role in astrophysics. *Phys.*

Rep., 178, 25.

Robert, P., et al. (1998), Tetrahedron geometric factors, in *Analysis Methods for Multi-Spacecraft Data*, edited by G. Paschmann and P. W. Daly, p. 323, ESA Publications Division, Noordwijk, The Netherlands.

Shen, C., X. Li, M. Dunlop, Z. X. Liu, A. Balogh, D. N. Baker, M. Hapgood, and X. Wang (2003), Analyses on the geometrical structure of magnetic field in the current sheet based on cluster measurements, *J. Geophys. Res.*, *108*(A5), 1168, doi:10.1029/2002JA009612.

Shen, C., Dunlop, M., Li, X., Liu, Z. X., Balogh, A., Zhang, T. L., Carr, C. M., Shi, Q. Q., and Chen, Z. Q. (2007), New approach for determining the normal of the bow shock based on Cluster four-point magnetic field measurements, *J. Geophys. Res.*, *112*, A03201, doi:10.1029/2006JA011699.

Shen, C., Zhou, Y. F., Ma, Y. H., Wang, X. G., Pu, Z. Y., Dunlop, M. (2021), A general algorithm for the linear and quadratic gradients of physical quantities based on 10 or more point measurements, *Journal of Geophysical Research: Space Physics*, *126*, e2021JA029121. <https://doi.org/10.1029/2021JA029121>.

Shen, X. H., Zhang, X. M., Yuan, S. G., Wang, L. W., Cao, J. B., Huang, J. P., Zhu, X. H., Piergiorgio, P., Dai, J. P. (2018). The state-of-the-art of the China Seismo-Electromagnetic Satellite mission. *Sci. China Technol. Sci.*, *8*, 61(5), 634–642. <https://doi.org/10.1007/s11431-018-9242-0>

Tong, Y., Vasko, I., Mozer, F. S., Bale, S. D., Roth, I., Artemyev, A. V., et al. (2018).

Simultaneous Multispacecraft Probing of Electron Phase Space Holes.

Geophysical Research Letters, 45(21), 11,511-

513,519. <https://doi.org/10.1029/2018GL079044>.

Torbert, R. B., Russell, C. T., Magnes, W., Ergun, R. E., Lindqvist, P.-A., LeContel, O.,
et al. (2016), The FIELDS Instrument Suite on MMS: Scientific objectives,
measurements, and data products. *Space Science Reviews*, 199, 105–135.

<https://doi.org/10.1007/s11214-014-0109-8>

Treumann, R. A., and Baumjohann, W. (1997). *Advanced Space Plasma Physics*. p. 31-
33, 155-167. Imperial College Press, 516 Sherfield Building, Imperial College,
London.

Yau, A. W., Takumi, A., and Peterson, W. K. (2007). The polar wind: Recent
observations[J]. *Journal of Atmospheric and Solar-Terrestrial Physics*, 69, 1936-
1983.

Figure Captions

Figure 1. A schematic view of the measurements of the electric field by the MMS constellation and the calculation of the charge density.

Figure 2. The structure of the magnetopause during an MMS crossing event on 11 November 2015. From top to bottom: (a) the magnetic flux density at the center of the constellation, (b) the electric-field at the center of the constellation, (c) the electron and ion number densities measured by MMS-1 (Pollock et al., 2016), (d) the rotation rates of the magnetic field (Shen et al., 2007), (e) $|\nabla|\mathbf{B}||$, (f) the radius of curvature of the magnetic field lines (Shen et al., 2003), and (g) the charge distribution. The red vertical line marks the largest rotation rates, and the black vertical dotted lines mark the largest and the smallest charge densities.

Figure 3. The distribution of the 10 probes.

Figure 4. The relative errors of the linear (a) and the quadratic (b) electric potential gradients, i.e., $\partial_x\phi$ and $\partial_x\partial_x\phi$, calculated for different numbers of iterations at $[0.1, 0, 0]$ within the uniformly charged ball.

Figure 5. The variation of the errors of the calculation by using the 10-probe scheme with the relative measurement scale L/D for the case of a uniformly charged ball. The measurements are performed inside of the charged ball. The left panels, (a), (c), and (e), show the truncation errors for the non-vanishing component of the linear gradient by L/D calculated for three different locations of the barycenter of the 10 probes inside the ball, $[0.1,0,0]$, $[0.4,0,0]$, and $[0.7,0,0]$. The right panels, (b), (d), and (f), illustrate the relative errors of the non-vanishing components of the quadratic gradient and charge density (dashed line) calculated for the same three locations of the barycenter. It is noted that $\phi_{,1} \equiv \partial_x \phi$ and $\phi_{,2,2} \equiv \partial_y \partial_y \phi$, where a comma denotes partial differentiation.

Figure 6. The dependence of the truncation errors of the calculations by using the 10-probe scheme on the relative measurement scale L/D for the case of a uniformly charged ball. The measurements are performed outside of the charged ball. The left panels, (a), (c), and (e), show the truncation error for the non-vanishing component of the linear gradient as a function of L/D calculated for three different locations of the barycenter of the 10 probes outside of the ball, $[3,0,0]$, $[5,0,0]$, and $[8,0,0]$. The right panels, (b), (d), and (f), illustrate the relative errors of the non-vanishing components of the quadratic gradient and the absolute value of the charge density (dashed line) calculated for the same three locations of the barycenter. It is noted that the real charge density outside of the ball is zero.

Figure 7. The relation between the absolute error of the charge density and the number of measurement points at $[3,0,0]$. The relative measurement scale is chosen as $L/D = 0.05$ (left) and $L/D = 0.01$ (right). The dashed lines are fitted from the modeled errors.

Figure 8. A schematic view of the seven-probe measurement of the charge density. The probes are indicated by black dots.

Figure 9. A schematic view of the eight-probe measurement of charge density.

Figure 10. The dependence of the truncation errors of the calculations by using the 8-probe scheme on the relative measurement scale L/D for the case of a uniformly charged ball. Panel (a) and (b) show the relative truncation errors of the quadratic gradient of the electric potential (solid lines) and the charge density (dashed lines) at $[0.5,0,0]$ and $[0.5,0.4,0.3]$ in the ball, respectively. Panel (c) and (d) show the relative truncation errors of the quadratic gradient of the electric potential (solid lines and left vertical axis) and the absolute errors of the charge density (dashed lines and right vertical axis) at $[8,0,0]$ and $[2,2,6]$ out of the ball. In panel (c), the orange line is overlaid with the green line. In panel (d), the blue line is overlaid with the orange line.